NOAA-20 VIIRS Polarization Effect and Its Correction

JUNQIANG SUN,[1,*] MENGHUA WANG,[2] LIDE JIANG,[2,3] AND XIAOXIONG XIONG[4]

[1]*Science Systems and Applications, Inc., 10210 Greenbelt Road, Lanham, MD 20706, USA*
[2]*NOAA National Environmental Satellite, Data, and Information Service, Center for Satellite Applications and Research E/RA3, 5830 University Research Ct., College Park, MD 20740, USA*
[3]*Cooperative Institute for Research in the Atmosphere, Colorado State University, Fort Collins, CO 80523 USA*
[4]*Science Exploration Directorate, NASA/GSFC, Greenbelt, MD 20771, USA*
**Corresponding author: junqiang.sun@noaa.gov*

Received XX Month XXXX; revised XX Month, XXXX; accepted XX Month XXXX; posted XX Month XXXX (Doc. ID XXXXX); published XX Month XXXX

The follow-on Visible Infrared Imaging Radiometer Suite (VIIRS) housed in the NOAA-20 satellite was launched on 18 November 2017. It has 22 spectral bands, among which 14 are reflective solar bands (RSBs) covering the wavelength range from 411 to 2258 nm. Prelaunch polarization sensitivity measurements have revealed that NOAA-20 VIIRS RSBs are much more sensitive to polarization of the incident light than its predecessor, the VIIRS on the Suomi National Polar-orbiting Partnership (SNPP). For the short wavelength bands, i.e., M1–M4, the polarization sensitivities are out of specifications, especially for the band M1, for which the polarization factors can be as large as ~6%. The polarization effect induces striping in imagery along the track and radiometric bias both along the scan and along the track, resulting in much larger uncertainties in the environmental data records (EDR). In this paper, the polarization effect correction algorithms are described and applied to the NOAA-20 VIIRS RSBs for ocean scenes where the top-of-atmosphere (TOA) radiance can be separated into the ocean normalized water-leaving radiance, the basis of the ocean color EDR, and the sunlight reflected by the atmosphere which can be mostly described by the Rayleigh scattering radiance. The errors of the sensor data records (SDR or Level-1B radiance) due to the polarization effect can be as large as ~1% for bands M1 and M2 and those in the ocean normalized water-leaving radiances are about 13% and 10% for wavelengths at 411 nm (band M1) and 445 nm (band M2), respectively. The polarization effect also induces strong striping in both NOAA-20 VIIRS RSB SDR and normalized water-leaving radiances. It is demonstrated that with the polarization correction applied, the aforementioned errors and artifacts are successful removed.

OCIS codes: *(280.0280) Remote sensing and sensors; (120.0120) Instrumentation, measurement, and metrology; (010.0010) Atmospheric and oceanic optics.*

http://dx.doi.org/10.1364/AO.99.099999

1. INTRODUCTION

The Visible Infrared Imaging Radiometer Suite (VIIRS) onboard the NOAA-20 satellite was launched on 18 November 2017. VIIRS, a scanning radiometer with a scan angle range of ±56.28° for the Earth view (EV), has 22 spectral bands covering a wavelength range from 0.411 to 12.49 μm [1,2]. NOAA-20 VIIRS began its daily collection of visible and infrared imagery and radiometric measurements of the land, atmosphere, cryosphere, and oceans on 3 December 2017. The data of NOAA-20 VIIRS as well as those of the precursor VIIRS onboard the Suomi National Polar-orbiting Partnership (SNPP) satellite are critically important for improving our understanding of global climate change [3]. In particular, VIIRS ocean color data [4] are important for monitoring and understanding of optical, biological, and biogeochemical processes and phenomena over global open oceans and coastal/inland waters [5-7].

Among the VIIRS 22 spectral bands, 14 are reflective solar bands (RSBs). The wavelengths and main specifications for NOAA-20 VIIRS RSBs are listed in Table 1. The RSBs are calibrated on-orbit using a solar diffuser (SD) with a solar diffuser stability monitor (SDSM) [8-15]. Near-monthly lunar observations are also utilized [16,17]. In the calibration methodologies, the incident light is assumed to be unpolarized and, thus, both the SD/SDSM calibration and the lunar calibration can only provide the calibration coefficients for the RSBs in the case when the incident light is unpolarized. However, the sunlight reflected from the Earth surface can be strongly polarized at various regions on the Earth surface and the degree of polarization of the sunlight can vary with scene [18-22].

The impact of the polarization effect on the collected data of a remote sensor depends on both the polarization sensitivity of an instrument and the polarization of the light reflected from the Earth surface [23-26]. The polarization sensitivity of the instrument is described by two parameters, polarization factor and polarization phase angle [27-30].

To constrain the uncertainty of the instrument due to polarization effect, the polarization sensitivity for each of the RSBs is specified. The specification as listed in Table 1 for VIIRS RSBs is that the polarization factor should be smaller than 3% for 411 nm (M1) and 868 nm (M7 and I2) bands and 2.5% for other RSBs for the scan angle within the scan angle range of ±45° [31]. There is no specification for the scan angle beyond the aforementioned range. It is also required that the uncertainty of the measured polarization factors should be less than 0.5% [31].

The VIIRS on NOAA-20 (called Joint Polar Satellite System (JPSS)-1 before reaching the final orbit) polarization sensitivity was measured prelaunch [32]. The measured polarization factors and phase angles depend strongly on band (wavelength), detector, and scan angle [29,30]. It was identified that several RSBs are much more sensitive to the polarization than the specification, especially for band M1 at 411 nm and band M4 at 556 nm, for which the polarization factors can be as large as ~6% and ~4%, respectively. They are also extremely sensitive to polarization than SNPP VIIRS RSBs whose polarization sensitivities are all within the specification [28]. Nevertheless, the polarization sensitivity of NOAA-20 VIIRS is at about the same level compared to the two Moderate Resolution Imaging Spectroradiometer (MODIS) instruments, one onboard the Terra satellite and another onboard the Aqua satellite, at their prelaunch stage and in early mission [27]. The polarization sensitivity of a satellite sensor may vary on-orbit due to the degradation of the instrument's optical components. For example, the Terra MODIS became much more sensitive to polarization after it passed its designed six-year lifetime on-orbit [22].

The polarization of the reflected sunlight from the Earth surface varies with scene and the reflected sunlight can cause significant striping along track in the NOAA-20 VIIRS SDR products due to detector dependence of the polarization sensitivity for each of the RSBs. It also induces radiometric bias in the SDR along the scan due to the scan angle dependence of the polarization sensitivity. The striping and bias further enhance the complexity of the scene dependence of the polarization effect in the SDR products. These errors are inherited and may be amplified in the environmental data records (EDR) and other higher-level science products. The band dependency of the polarization sensitivity brings further complexity and errors for the EDR products that are derived using the radiance differences between two different bands. For achieving good accuracy in the SDR products, EDR products, and higher-level science products, it is necessary and critical to correct or removal of the polarization effect in the NOAA-20 VIIRS SDR and then in the EDR products.

The polarization effect depends on both the polarization sensitivity of the instrument and the polarization of the incident light as mentioned above [23-26]. To correct the polarization effect in the SDR products, both the polarization sensitivity of the instrument and the polarization of the incident light are required. The polarization sensitivity of NOAA-20 VIIRS was characterized prelaunch as previously mentioned [29,30]. It may change on-orbit as observed in the Terra MODIS [22], but it should be stable in early mission. Thus, the prelaunch measured polarization factors and phase angles can be used for the correction. The description of the polarization of the sunlight reflected from the Earth surface is a very challenge issue, although there are satellite sensors designed to measure the polarization of the reflected sunlight and there are numerous models to predict the polarization of the sunlight [33-38]. The polarization of the reflected sunlight is scene dependent as mentioned above and is quite different for different types of Earth surface [39,40]. For an ocean scene, the reflected sunlight at the top of atmosphere (TOA) is generally dominated by Rayleigh scattering of atmosphere (particularly at the short visible bands) due to strong absorption of ocean and thus the polarization of the reflected sunlight can be well described by considering Rayleigh scattering [41-47], although there are also some less significant aerosol polarization effects [26].

In this paper, we apply the polarization correction to NOAA-20 RSBs SDR for ocean scenes and show that the polarization effect on RSBs can be removed despite the polarization sensitivity of the RSBs being much larger than the designed polarization sensitivity specification. In Section 2, the polarization effect and its correction are briefly described. In Section 3, the polarization sensitivity of NOAA-20 is concisely reviewed. In Section 4, the Rayleigh scattering applied in this analysis is presented. In Section 5, the impact of the polarization effect in NOAA-20 VIIRS RSB SDR and ocean color EDR products is displayed and the successful removal of the polarization effect in the products is demonstrated. Finally, Section 6 summarizes this analysis and concludes the paper.

Table 1. Polarization sensitivity and its characterization uncertainty specification for NOAA-20 VIIRS visible and near infrared bands.

Band	Wavelength (nm)	Maximum Aplitude for within ±45° Scan angle
M1	411	3
M2	445	2.5
M3	489	2.5
M4	556	2.5
M5	667	2.5
M6	746	2.5
M7	868	3
I1	642	2.5
I2	868	3

2. POLARIZATION FORMULISM

A monochromatic linear polarized light beam can be described by a plane wave. In a coordinate system with z-axis pointing along the direction of light propagation, the electric field vector of the linear polarized light can be written as [23,24,27]

$$\mathbf{E} = \begin{pmatrix} \cos(\alpha) \\ \sin(\alpha) \end{pmatrix} E , \quad (1)$$

where E is the amplitude of the electric field, α is the angle between the direction of the electronic field and the x-axis and is called polarization angle. When the light passes through an optical system, the electric field at each optical surface changes, and at the detector the beam of light $\mathbf{E}'$ can be related to the incident electric field $\mathbf{E}$ by a two-dimensional Jones matrix $\mathbf{U}$ [23] by

$$\mathbf{E}' = \mathbf{U}\mathbf{E}. \quad (2)$$

The radiance of the light after passing the optical system is then given by

$$I' = \mathbf{E}^{\dagger}\mathbf{H}\mathbf{E} , \quad (3)$$

where $\mathbf{E}^{\dagger}$ is the conjugate transpose of $\mathbf{E}$ and

$$\mathbf{H} = \mathbf{U}^{\dagger}\mathbf{U} \quad (4)$$

is a two-dimensional Hermitian matrix. Eq. (4) can be further written as [16]

$$I' = hI\{1 + a\cos[2(\alpha - \delta)]\}, \quad (5)$$

where h is the averaged transmittance of the optical system, a is the polarization factor, δ is the polarization phase angle, and

$$I = \mathbf{E}^{\dagger}\mathbf{E}, \quad (6)$$

is the radiance of the light before passing the optical system. The radiance I' varies with the polarization angle and reaches its maximum when the polarization angle is same as the polarization phase angle δ. The polarization effect depends on the difference between α and δ, which is independent of the coordinate system, provided that they are determined in the same system.

Sunlight coming directly from the Sun is not polarized and its electric field has a random distribution in the plane perpendicular to the direction of propagation. However, sunlight reflected from the Earth scene becomes partially polarized due to Rayleigh scattering, surface reflection, and other effects. For the partially polarized light, the radiance after it passes the optical system can still be expressed in an analytical form [27]

$$I' = hI\{1 + fa\cos[2(\mu - \delta)]\}, \quad (7)$$

where f is the scene polarization factor that measures the degree of polarization of the incident light and μ is the angle between the direction, along which electric field has the largest distribution, and that of the x-axis. The scene polarization factor equals 0 when the scene is not polarized, while approaches 1 when it is fully polarized.

A polarized light, especially partially polarized light, can also be described using a Stokes vector [23-25]

$$\mathbf{I} = \begin{pmatrix} I \\ Q \\ U \\ V \end{pmatrix}, \quad (8)$$

where I, Q, U, V are Stokes parameters and I is the radiance of the light same as that expressed in Eq. (6). The effect of the optical system on the Stoke vector **I** is described by a Mueller matrix and the Stoke vector, **I**′, for the light passing the optical system as [23]

$$\mathbf{I}' = \mathbf{M}\mathbf{I}, \quad (9)$$

where **M** is a 4×4 matrix. Then the radiance of the light after it passes the optical system can be expressed as

$$I' = M_{11}I(1 + m_{12}q + m_{13}u), \quad (10)$$

where M_{11} is the first element in the first row of the Mueller matrix, m_{12} and m_{13} are second and third elements normalized by M_{11} and q and u are the ratios of Q and U over I.

By comparing Eqs. (7) and (10), the relationship between the two sets of parameters and quantities in the two equations can be easily established. The two polarization parameters of the optical system in the two descriptions are related by

$$m_{12} = a\cos(2\delta), \quad m_{13} = a\sin(2\delta). \quad (11)$$

The polarization of the Earth surface reflection is usually described by a Stokes vector, while the polarization sensitivity of a remote sensor is characterized by polarization factor and phase angle. In other words, the measured polarization factor and phase angle need to be transferred into the normalized Mueller matrix elements, m_{12} and m_{13}, by using Eq. (11) in order to apply the polarization effect to EV scene.

3. NOAA-20 VIIRS POLARIZATION SENSITIVITY

The polarization sensitivity of NOAA-20 VIIRS was measured prelaunch by the sensor vendor (Raytheon El Segundo) [29,30]. The polarized light source was provided by a so-called the polarization test source assembly (PTSA), the two major parts of which were a spherical integration source (SIS) and a polarizing sheet. The former provides unpolarized illumination at its exit aperture and the latter only allows the light vibrates in one direction to pass and then produces a linearly polarized light. The polarizing sheet is mounted to a rotation stage which can rotate 360° to allow the sensitivities of the NOAA-20 VIIRS RSB responses to a specified polarization direction of a linear polarized light to be measured. The results of the measurements show that the NOAA-20 VIIRS polarization sensitivities were much larger than its predecessor on the SNPP spacecraft and fail the sensor requirements of ~2.5–3% [30]. An additional test was performed using a monochromatic source. Specifically, the National Institute of Standards and Technology's (NIST's) Traveling Spectral Irradiance and Radiance Responsivity Calibrations Using Uniform Sources (T-SIRCUS) was implemented, and confirmed the results of the test using the PTSA as light source [29]. A simulation using a ray trace model was also performed to provide more insight about the large polarization sensitivities of the RSBs [48].

In this analysis, the polarization factors and phase angles measured using the PTSA are used to describe the polarization sensitivities of the NOAA-20 VIIRS RSBs. Figure 1 shows the polarization factors for all detectors and HAM side of the visible and near-infrared (NIR) bands. The polarization sensitivity of the instrument was measured at 11 different scan angles: -55°, -45°, -37°, -30°, -20°, -15°, -8°, 4°, 22°, 45°, and 45°. Same symbols with a given color represent the polarization factors measured at the same scan angle which is shown in the right side of the plot. The x-axis is the counting of detector, HAM side, and band with detector changing first starting from detector 1, then HAM side changing starting from HAM side 1, and finally band changing starting from I1. It can be seen clearly that the polarization factors are strongly band, detector, and scan angle dependent. They also depend on the half angle mirror (HAM) side, but the dependency is much weaker. For most of bands, the polarization factors are much larger than the specification listed in Table 1. In particular, the band M1 has the largest polarization sensitivity among all bands, which can be as large as ~6%. The polarization sensitivity decreases with the increase of the wavelength for the visible bands except for the band M4, which has unexpectedly much larger polarization sensitivity than those of bands M2 and M3. Band M4 is one of the most important bands among all RSBs for ocean color EDR products. The polarization phase angles of the NOAA-20 VIIRS RSBs are also strongly dependent on band, detector, and scan angle.

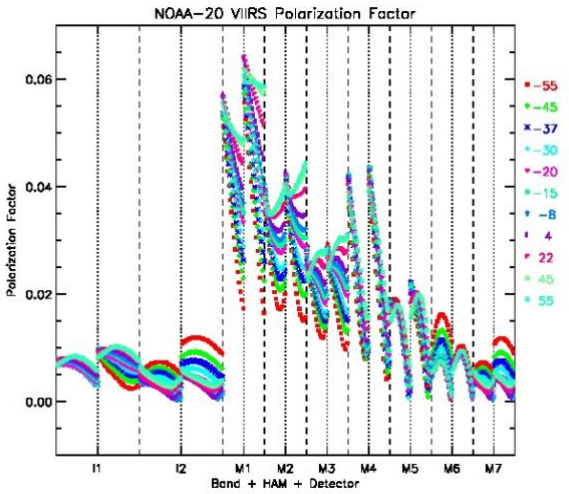

Fig. 1. Polarization factors for NOAA-20 VIIRS (JPSS-1) VisNIR bands: Left side of the dotted line for HAM A and the other side for HAM B. The numbers on the right side are the scan angles. The symbols with the same color of a scan angle at the right side represent the polarization factors measured at the scan angle. "Band + HAM + Detector" in x-axis is the counting of the detectors starting from band I1, HAM side 1, and detector 1.

With the polarization factors and phase angles, the normalized elements of the Mueller matrix, m_{12} and m_{13}, can be easily calculated by using Eq. (11). Fig. 2 shows both m_{12} and m_{13} for all detectors of NOAA-20 VIIRS band M1, where symbols are the values calculated from the measured polarization factors, shown in Fig. 1, and phase angles. The symbols are measured values and different symbols belong to different detectors. The values of each detector are presented using the same symbols and same color. The measured polarization parameters, either m_{12} or m_{13}, for each detector and HAM side are fitted to a quadratic form of scan angle. The solid lines are fitted m_{12}, while the dashed lines are fitted m_{13}. The former is almost the same for all detectors, while the latter is strongly detector dependent. From both Figs. 1 and 2, it is seen that detector 1 is the most sensitive to the polarization effect, while detector is less affected by the polarization effect. Figure 3 shows m_{12} and m_{13} for the band M2. Same as band M1, m_{12} values are about the same for all detectors, while m_{13} change dramatically with detector. As mentioned previously, band M2 is less sensitive to the polarization of the incident light than band M1. Both bands M1 and M2 are more sensitive to the polarization effect than their polarization specification [31]. Similarly, one can calculate the two Mueller matrix elements for all visible and NIR bands. They are also more sensitive to the polarization effect than their counterparts in SNPP VIIRS.

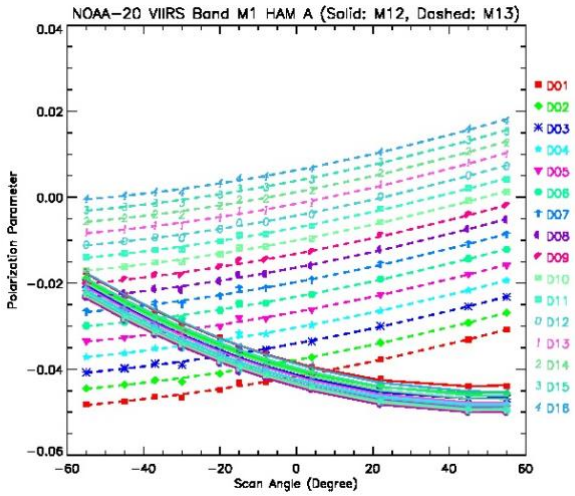

Fig. 2. NOAA-20 VIIRS band M1 polarization parameters: m_{12} (solid lines) and m_{13} (dashed lines). The numbers D1-D16 on the right side represent detectors 1-16.

+

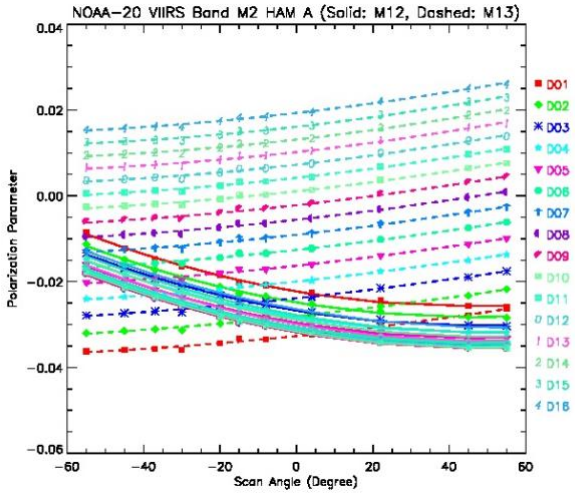

Fig. 3. NOAA-20 VIIRS band M2 polarization parameters: m_{12} (solid lines) and m_{13} (dashed lines).

4. RAYLEIGH SCATTERING RADIANCE

The polarization of the sunlight reflected from the Earth surface is strongly scene dependent. It not only depends on the type of surface, but also the viewing geometry including the position of the Sun, geolocation of the spot observed, and the position of the instrument at the time of the observation. For this analysis, we focus on ocean scenes.

For ocean scenes, by ignoring ocean whitecap and sunglint contributions [49,51], the TOA radiance, L_{top}, composes of two major parts, the radiance reflected by the atmosphere (and ocean surface) and that by the ocean. Then we can write

$$L_{top} = L_{atm} + t\, t_0 \cos\theta_0\, nL_w, \quad \textbf{(12)}$$

where L_{atm} is the radiance reflected or scattered by the atmosphere (including both molecules and aerosols) and nL_w is the normalized water-leaving radiance [51,52], t and t_0 are the

atmospheric diffuse transmittance at the sensor and solar direction, respectively [52], and θ_0 is solar-zenith angle. It is noted that in the above equation ocean whitecap radiance [51] (generally small) and sunglint contributions [49] (need to be avoided in ocean color remote sensing) are ignored.

For a clear sky, the sunlight reflected by the atmosphere, L_{atm}, is mainly the Rayleigh scattering radiance (particularly for the short visible bands), which is the scattering of light off of the molecules of the air [41-47]. Rayleigh has derived an analytical expression for the Rayleigh scattering radiance based on the approximation that the molecules in the air are simple dipole scatters and their sizes are much smaller than the wavelength of the light [41-42]. The Rayleigh scattering radiance strongly depends on wavelength and is inversely proportional to the fourth order of the wavelength [41-43]. In addition, light scattered by molecules (Rayleigh scattering) is strongly polarized (almost completely polarized at the 90^0 scattering angle). Thus, it has much more important impact on light with shorter wavelength such as blue light than that with longer wavelength such as red light, due to much larger Rayleigh radiance magnitude at the short visible bands. It also depends on the viewing geometry as aforementioned.

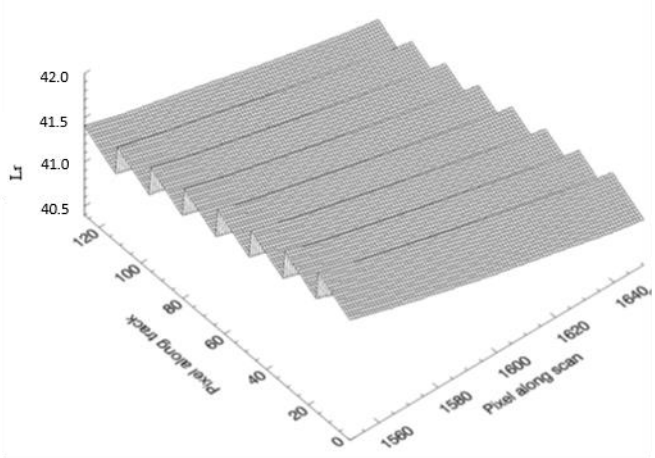

Fig. 4. L_r component of Rayleigh scattering Stokes vector for a scene observed by NOAA-20 VIIRS band M1 around 5 PM on February 4, 2018 in North Pacific Ocean.

The Rayleigh scattering model has been continuously improved in the past more than a century and has been widely used to simulate the radiance of the sunlight reflected by the atmosphere. In this analysis, we use the model widely used in the ocean color community to calculate the Rayleigh scattering radiance [45-47]. In particular, Rayleigh radiances computed from Wang (2016) [47] for VIIRS are used. Since the Rayleigh scattering radiance is strongly polarized, it is described by a Stokes vector in the model (for Rayleigh scattering), e.g.,

$$\boldsymbol{L}_{atm} = \begin{pmatrix} L_r \\ L_q \\ L_u \\ L_v \end{pmatrix}, \qquad \textbf{(13)}$$

where L_r, L_q, L_u, and L_v are the Stokes parameters, corresponding to I, Q, U, V components in Eq. (8), respectively.

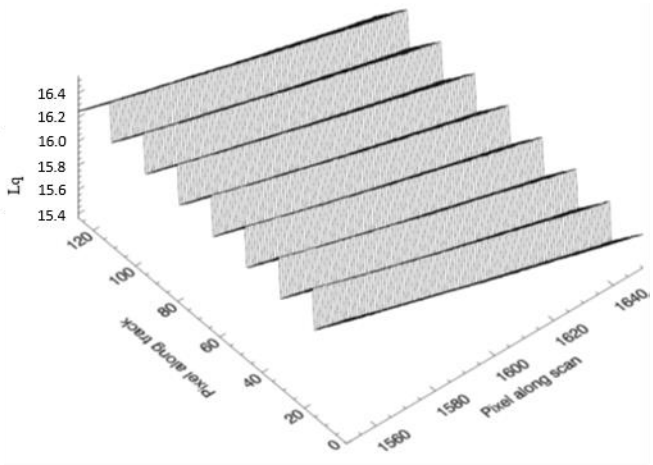

Fig. 5. L_q component of Rayleigh scattering Stokes vector for a scene observed by NOAA-20 VIIRS band M1 around 5 PM on February 4, 2018 in North Pacific Ocean.

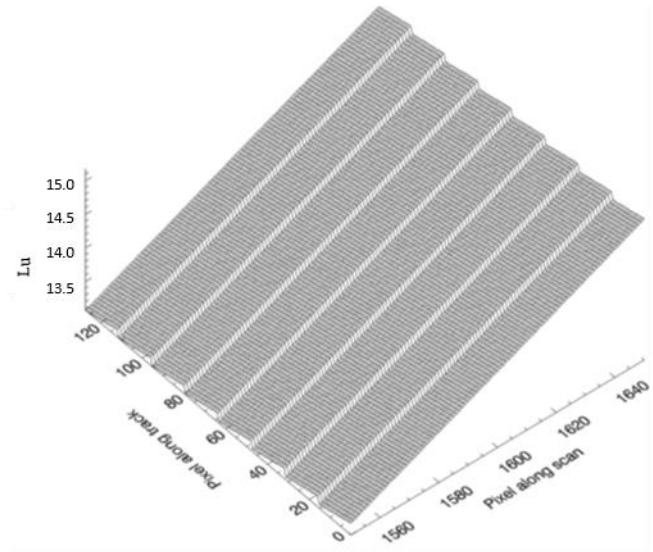

Fig. 6. L_u component of Rayleigh scattering Stokes vector for a scene observed by NOAA-20 VIIRS band M1 around 5 PM on February 4, 2018 in North Pacific Ocean.

NOAA-20 VIIRS flew over North Pacific Ocean around 5 PM on February 4, 2018. Figure 4 shows the simulated Rayleigh radiance, L_r, for the observation directions of the 16 detectors of NOAA-20 VIIRS band M1 at wavelength of 411 nm. In this three-dimensional surface, the x-axis is along scan direction and the y-axis is along track direction. Along the scan direction, band M1 has a total of 3200 pixels (aggregated) in the Earth view (EV) sector. In Fig. 4, only results for the center 1000 pixels are shown. Along the track direction, there are 16 pixels in each scan since there are 16 detectors in band M1. In Fig. 4, only the results of first 8 scans are shown. The image shows that the Rayleigh radiance varies with geolocation or viewing geometry as expected. A clear discontinuity from one scan to next is seen in Fig. 4. This is due to the different viewing directions of the 16 detectors along track, inducing a discontinuity in the viewing geometry from detector 16 in the previous scan to that of detector 1 in the next. In other words, Rayleigh scattering

radiance, which definitely has contribution to the TOA radiance observed by a VIIRS instrument for any EV scene, introduces striping to the VIIRS EV imagery due to viewing geometry differences of the detectors in the same band.

Figures 5 and 6 show the L_q and L_u components of the Stokes vector of Rayleigh scattering radiance for the same scene as the L_r component shown in Fig. 4. The discontinuities are clearly observed between two adjacent scans in both components for the same reason that induces the discontinuity in L_r imagery as shown in Fig. 4. From Figs. 4-6, it can be seen that L_q and L_u together have similar magnitude as L_r. This indicates that the Rayleigh scattering radiance is indeed polarized and polarization is significant. The two images demonstrate that, same as L_r, L_q and L_u vary with viewing geometry. Furthermore, L_u continuously increases along the scan. In other words, it becomes larger as increase of the scan angle.

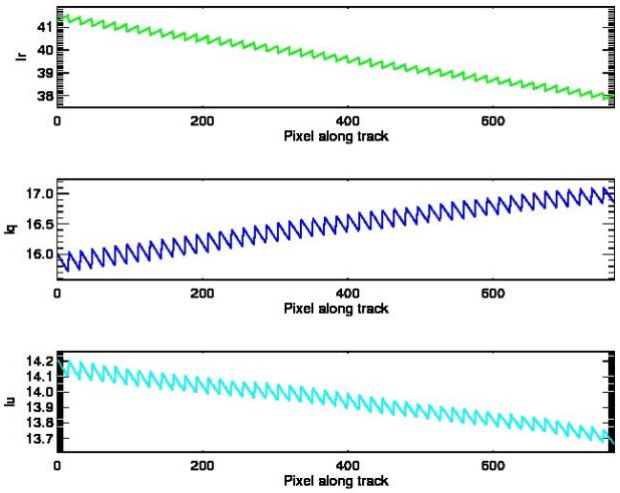

Fig. 7. Profiles of L_r, L_q, and L_u along track for 48 scans with a pixel number of 1600 along scan.

The profiles of L_r, L_q, and L_u along the track for 48 scans with a pixel number of 1600 along the scan are displayed in Fig. 7. The data in the profiles are the same data shown in Figs. 4-6. The zigzag pattern in the profiles is due to the differences in the viewing geometries of the 16 detectors as discussed previously. NOAA-20 flies always toward north at the dayside of the Earth and thus the latitude of the pixel along the track increases with the pixel number (x-axis). Since the scene is in the North Pacific Ocean, the radiance of the sunlight reflected from the Earth surface should decrease with the increasing latitude. The top and bottom charts in Fig. 7 show that Rayleigh scattering radiance, L_r, and the L_u component do decrease with the increase of latitude as expected. However, opposite to L_r and L_u, L_q increases with the increase of latitude as shown in middle chart in Fig. 7. This indicates that Rayleigh scattering radiance becomes more polarized at higher latitudes.

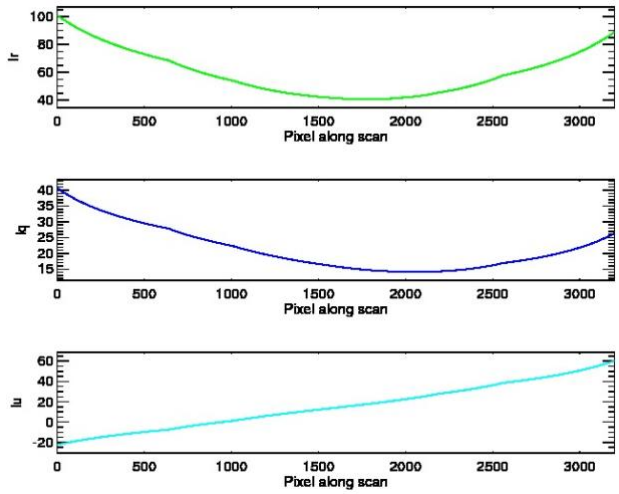

Fig. 8. Profiles of L_r, L_q, and L_u along the scan.

The profiles of L_r, L_q, and L_u along the scan are displayed in Fig. 8. Same as the profiles in Fig. 7, the data in these profiles are the same data shown in Figs. 4-6. It is demonstrated in the profiles that Rayleigh scattering radiances are larger at two ends of the scan while have its minimum at a spot close to nadir. The component L_q has a pattern similar to that of the radiance with its minimum shifted toward the end of the scan. The component L_u performs very differently from other two components. It continuously increases from the beginning of the scan to the end of the scan. This indicates that the degree of polarization for Rayleigh scattering is larger at the end of the scan than that at the beginning of the scan.

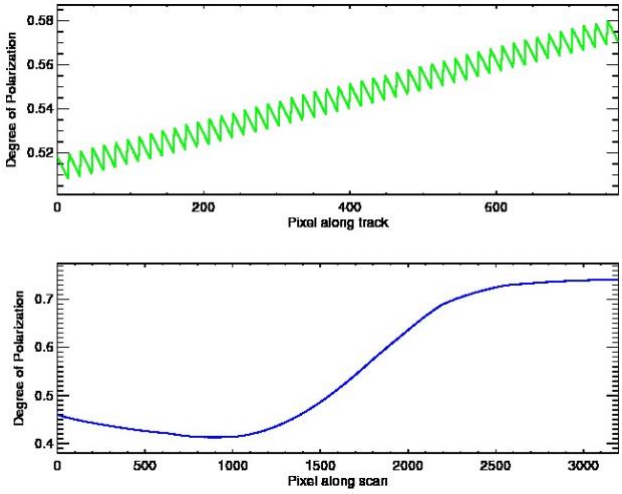

Fig. 9. Degree of polarization for the Rayleigh scattering at the wavelength of 411 nm.

The degree of polarization, the scene polarization factor f in Eq. (7), of the Rayleigh scattering radiance can be expressed as

$$f = \frac{\sqrt{L_q^2 + L_u^2}}{L_r}. \quad \textbf{(14)}$$

The top and bottom charts in Fig. 9 shows the degree of polarization for Rayleigh scattering radiance at the wavelength of 411 nm along the track and scan direction, respectively. It is seen from the top chart that the degree of polarization of Rayleigh scattering radiance at the wavelength of 411 nm continuously increases as the instrument orbits toward the northern pole. The bottom chart demonstrates that the degree of polarization is much larger at the second half of the scan than that at the first half of the scan. In other words, the degree of polarization for Rayleigh scattering radiance is much larger for forward scattering light than that for backward scattering light.

5. POLARIZATION EFFECT CORRECTION

The primary SDR products (L1B products in MODIS) of NOAA-20 VIIRS for a reflective solar band B are the EV radiance $L_{EV,B}$ and reflectance, $\rho_{EV,B}\cos(\theta_{EV})$, where ρ_{EV} is the Earth scene bi-directional reflectance factor (BRF) and θ_{EV} is the solar zenith angle of the Earth scene. The NOAA-20 VIIRS RSBs are calibrated using onboard SD and SDSM [9,53]. They are also calibrated using the scheduled lunar observations [54]. Both are considered to provide non-polarized light sources for the RSB calibration as mentioned previously. Thus, the SDR products are only accurate when sunlight reflected from the Earth surface is non-polarized or if the polarization effect is negligible. But, this is not the actual case as discussed previously. For sunlight reflected from the Earth surface, the actual EV radiance $L_{EV,B}$ and reflectance $\rho_{EV,B}$ can be related to the instrument measured radiance $L_{EV,B}^{SDR}$ and reflectance $\rho_{EV,B}^{SDR}$ for band B by

$$L_{EV,B}^{SDR} = L_{EV,B} C_{pl}(B, D, M, \phi) \quad (15)$$

and

$$\rho_{EV,B}^{SDR}\cos(\theta_{EV}) = \rho_{EV,B}\cos(\theta_{EV}) C_{pl}(B, D, M, \phi), \quad (16)$$

where

$$C_{pl}(B, D, M, \phi) = 1 + m_{12}q + m_{13}u \quad (17)$$

is the polarization correction factor according to Eq. (10). In the following discussion, we will focus on EV radiance, but the analysis is the same for the reflectance.

For an ocean scene, by combining Eqs. (12), (13), (15), (16) and (17), we can get

$$L_{EV,B}^{SDR} = tL_w + L_{atm} + m_{12}L_q + m_{13}L_u, \quad (18)$$

where L_a, L_q, and L_u are the first three components of the Stokes vector of Rayleigh scattering radiance as described in Eq. (13) and L_w is the ocean water-leaving radiance, i.e., $L_w = t_0 \cos\theta_0 \, nL_w$ from Eq. (12), where nL_w is normalized water-leaving radiance. The ocean normalized water-leaving radiance is considered to be nonpolarized or that the its polarization effect is negligible. For ocean color EDR, normalized water-leaving radiance is a fundamental quantity and the base for the entire EDR products. Eq. (18) can be rewritten as

$$nL_w = \left[L_{EV,B}^{SDR} - L_{atm} - m_{12}L_q - m_{13}L_u\right]/t\ t_0\cos\theta_0\,. \quad (19)$$

If the polarization effect is not considered or corrected, Eq. (19) can be simplified as

$$nL_w = \left[L_{EV,B}^{SDR} - L_{atm}\right]/t\ t_0\cos\theta_0\,. \quad (20)$$

In the following of this section, the impact of the polarization effect on the normalized water-leaving radiance and its correction will be demonstrated.

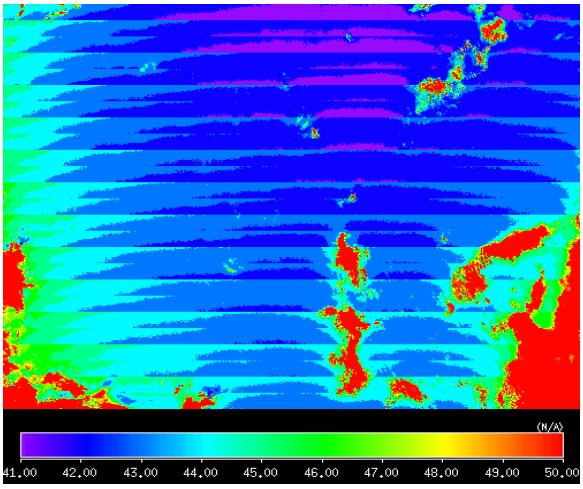

Fig. 10. NOAA-20 VIIRS band M1 IDPS for the time period around 5 PM (UTC) on February 4, 2018 in North Pacific Ocean.

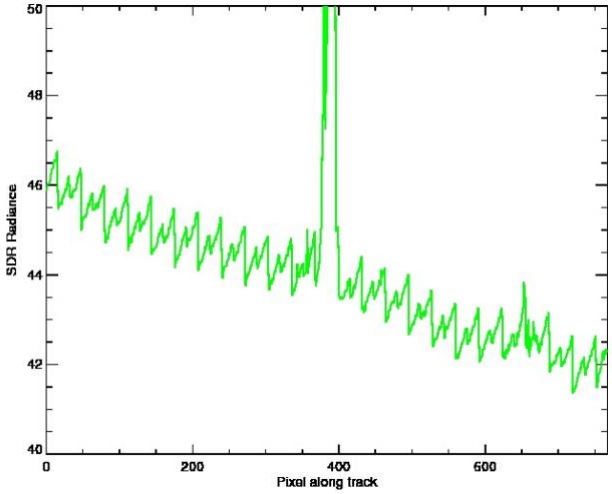

Fig. 11. NOAA-20 VIIRS band M1 SDR radiance (W/m^2-μm-sr) profile along the track direction at the center of the image in Fig. 10.

Figure 10 shows NOAA-20 VIIRS band M1 SDR radiance observed around 5:00 PM on February 4, 2018 in the North Pacific Ocean. The SDR radiance is generated by the Interface Data Processing Segment (IDPS) with the calibration coefficients provided by the VIIRS SDR team. In the image, striping along the track direction is clearly observed. To display the striping more clearly, Fig. 11 shows the profile of the radiance along the track direction passing through the center of the image in Fig. 10. The radiance along the track direction decreases, in general, with pixel number as expected since the instrument flew toward north in the northern hemisphere. However, there is a two-scan cycle. In each of the cycles, the radiance within first scan increases with detector number and then continuously increase in next scan. This means that there is a detector dependent striping and a HAM side dependent striping as well. The amplitude of the striping is about 2.2%, which is larger than the specification, 2%, of the SDR calibration specification their effects.

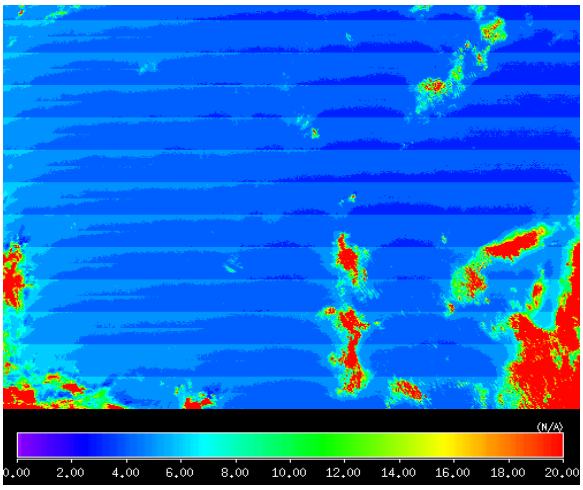

Fig. 12. Normalized water-leaving radiance at the M1 411 nm derived from the SDR shown in Fig. 10 without polarization correction applied.

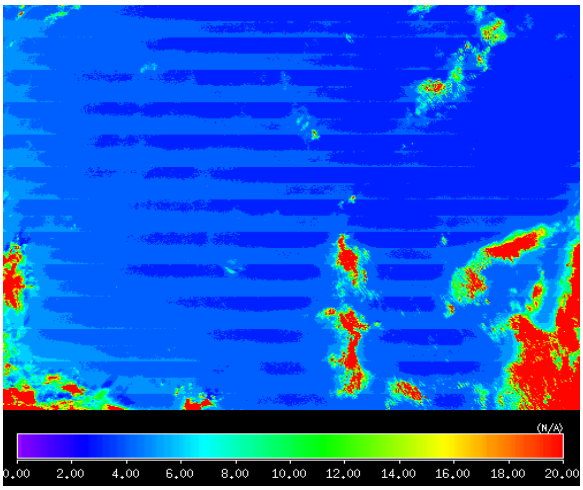

Fig. 13. Normalized water-leaving radiance at the band 411 nm derived from the SDR shown in Fig. 10 with polarization correction applied.

Figure 12 shows the normalized water-leaving radiance, calculated using Eq. (20), without the polarization effect correction applied. Similarly, as in SDR image in Fig. 10, the striping along track direction is clearly observed and the striping has a two-scan cycle pattern. Again, to see the striping more clearly, the profile of the normalized water-leaving radiance along the track direction at the center of the image in Fig. 12 is drawn as the red curve in Fig. 14. The amplitude of the striping is about 0.5 W/m^2-μm-sr, which is about half of that in the SDR profile shown in Fig. 11. The reduction of the absolute amplitude of the striping is due to the removal of the Rayleigh scattering radiance L_r, which has a detector dependent bias as discussed in previous section. However, the normalized water-leaving radiance L_w is about a magnitude smaller compared to the SDR radiance and thus the amplitude of the striping in the normalized water-leaving radiance becomes about five times larger in percentage, that is, about 11% as seen in Fig. 14. A striping effect with amplitude of 11% indicates that the uncertainty of the normalized water-leaving radiance is at least 11% since the striping only displays the relative uncertainties among detectors of the band.

Figure 13 shows the normalized water-leaving radiance after the polarization correction is applied. Striping is still observed in the image but the striping pattern has changed. The detector difference becomes smaller while the HAM side difference remains. To see the striping pattern change clearly, the profile of the normalized water-leaving radiance along track direction at the center of the image in Fig. 13 is displayed as green curve in Fig. 14. The detector difference is indeed significantly reduced. This is expected since the polarization sensitivity of NOAA-20 VIIRS band M1 is strongly detector dependent as shown in Fig. 1. However, the HAM side difference stays almost the same. As shown in Fig. 1, the polarization sensitivity of the band is about the same for the two HAM sides. This means that the polarization correction should not change the HAM side difference of the normalized water-leaving radiance. In other words, the HAM side difference in normalized water-leaving radiance is not induced by the polarization effect but by calibration errors. The HAM side difference in the normalized water-leaving radiance after the polarization effect corrected is about 11%. Considering that the normalized water-leaving radiance is about 10% of the SDR radiance, the relative error in the calibration coefficients used to generate the IDPS SDR for the two HAM sides is estimated to be 1.1%.

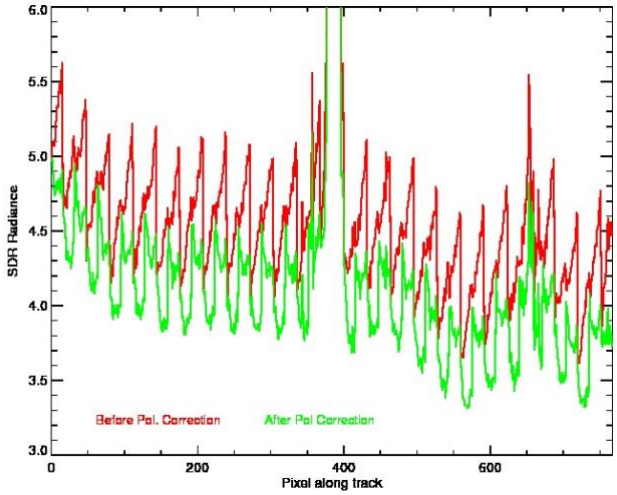

Fig. 14. Profiles of the normalized water-leaving radiance shown in Figs. 12 along the track direction at the center of the images in Figs. 12 and 13.

The normalized water-leaving radiance reduces about 12% on band average after the polarization correction applied according to the curves in Fig. 14. This also means that the SDR radiance has an error of 1.2% due to the polarization effect. The polarization effect is scene dependent. The effect may become smaller in equator area but definitely becomes larger in high latitude area. It may also be larger at large scan angle range since the polarization degree of the Rayleigh radiance are much larger at second half of the scan in the EV. Therefore, polarization correction is necessary for high quality and accurate of NOAA-20 band M1 ocean color EDR., and likely so for other EDRs.

It should be noted that, in deriving normalized water-leaving radiances (using atmospheric correction [50, 52, 55]) from the sensor-measured TOA radiances for global oceans, aerosol polarization effects are also fully accounted for [26]. The aerosol polarization effect on the satellite-derived normalized water-leaving radiances (or ocean color products) usually is not significant [26].

Figures 15, 16, and 17 show NOAA-20 band M2 IDPS SDR radiance, normalized water-leaving radiance before and after

polarization correction applied. Same as for band M1, striping with a pattern of two-scan cycle is observed in both the SDR radiance and the normalized water-leaving radiance without polarization correction applied. Similar to band M1 result, the detector dependent striping is greatly reduced while the HAM side dependent striping remains after the polarization correction is applied. Figures 18 and 19 display the profiles of the SDR radiance and normalized water-leaving radiance before and after polarization correction, respectively. It can be estimated from the two curves in Fig. 19 that the polarization effect makes the normalized water-leaving radiance and SDR radiance about 10% and 1%, respectively, higher than their actual values. The HAM side difference in the green curve, the normalized water-leaving radiance after polarization correction, indicates that there is a 1% relative calibration error between the two HAM sides.

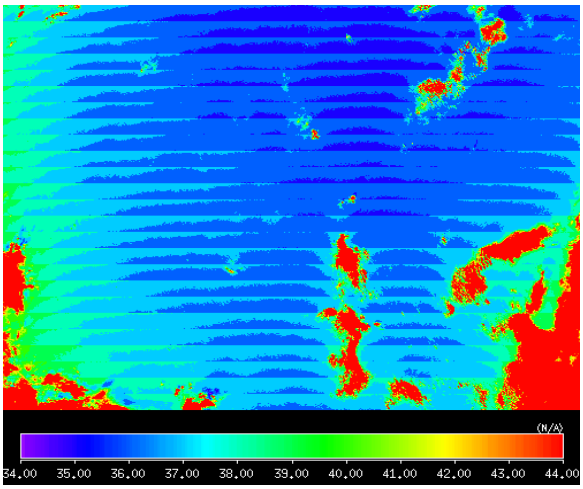

Fig. 15. NOAA-20 VIIRS band M2 IDPS for the time period around 5 PM (UTC) on February 4, 2018 in North Pacific Ocean.

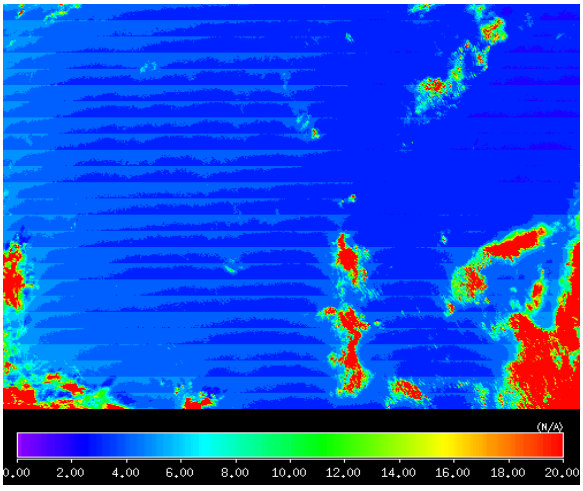

Fig. 16. Normalized water-leaving radiance at the band 445 nm derived from the SDR shown in Fig. 15 without polarization correction applied.

Same as bands M1 and M2, polarization effect induces detector dependent striping in all other NOAA-20 visible and near infrared bands. The amplitudes of the induced striping are different for different bands. They become smaller with increase of the band wavelength, except band M4 whose polarization factors are larger than those of band M3 as displayed in Fig. 1. The polarization correction has also been applied to all other visible and near infrared bands. The polarization effect has significant impacts in short wavelength bands but gradually becomes negligible with increasing the band wavelength.

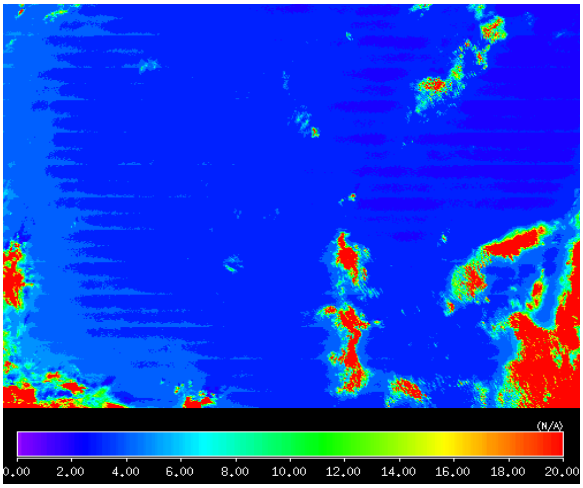

Fig. 17. Normalized water-leaving radiance at the M2 445 nm derived from the SDR shown in Fig. 15 with polarization correction applied.

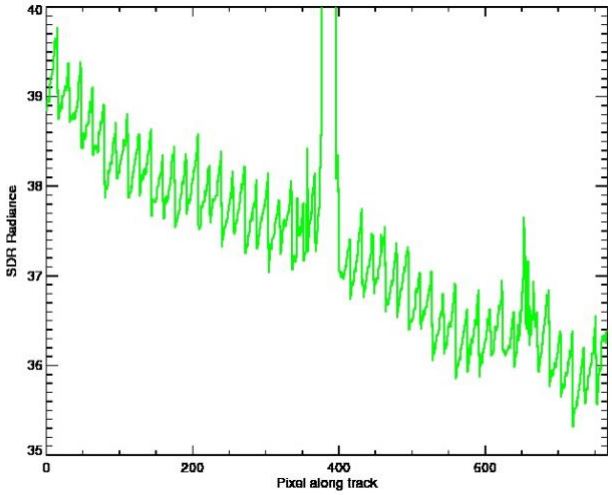

Fig. 18. NOAA-20 VIIRS band M2 SDR radiance profile along the track direction at the center of the image in Fig. 15.

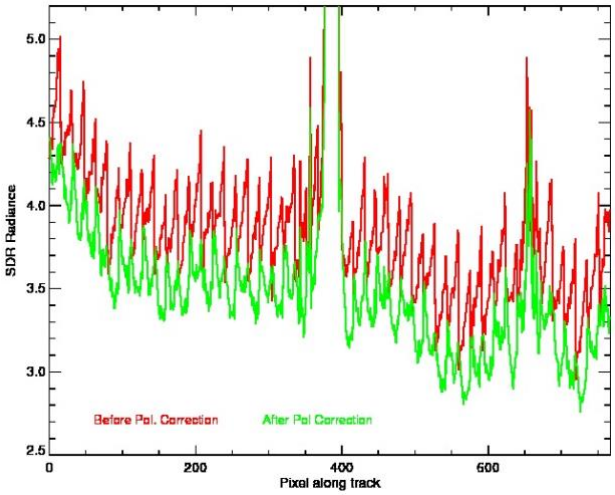

Fig. 19. Profiles of the normalized water-leaving radiance shown in Figs. 16 along the track direction at the center of the images in Figs. 18 and 13.

6. CONCLUSIONS

NOAA-20 VIIRS RSBs have much larger polarization effect compared to SNPP VIIRS RSBs. The polarization effect induces strong striping in EV imagery and scene dependent bias in radiometry. The polarization correction is applied to NOAA-20 RSBs for EV ocean scenes. It is demonstrated the polarization effect induces striping up to 2.2% and 11% effect in band M1 SDR radiance and normalized water-leaving radiance, respectively, for the ocean scenes. It also induces a radiometric bias around 1.1% and 11% in the SDR radiance and normalized water-leaving radiance, respectively. Both striping and the radiometric bias are strongly scene dependent and therefore can be much larger than the aforementioned values. For other short visible wavelength bands, the polarization effect has a similar level of impact. With polarization correction applied, the striping and the radiometric bias due to the polarization effect are removed. Since the errors induced by the polarization effect are larger than 10% in ocean normalized water-leaving radiance, the polarization correction is crucial for NOAA-20 ocean color EDR products. It is also shown that the current IDPS SDR products have a significant mirror side striping due to calibration error.

Funding Information. National Oceanic and Atmospheric Administration (NOAA) and National Aeronautics and Space Administration (NASA) Joint Polar Satellite System.

Acknowledgment. We would like to thank NASA VIIRS Characterization Support Team (VCST) for providing NOAA-20 VIIRS pre-launch polarization parameters and also to thank Dr. Sriharsha Madhavan (SSAI) for his helpful comments. This work was supported by the Joint Polar Satellite System (JPSS) funding. The views, opinions, and findings contained in this paper are those of the authors and should not be construed as an official NOAA or U.S. Government position, policy, or decision.

References

1. S. Mills, VIIRS Radiometric Calibration Algorithm Theoretical Basis Document, Doc. No.: D43777 (Northrop Grumman Aerospace Systems, 2010).
2. C. Cao, F. Deluccia, X. Xiong, R. Wolfe, and F. Weng, "Early on-orbit performance of the Visible Infrared Imaging Radiometer Suite (VIIRS) onboard the Suomi National Polar-orbiting Partnership (S-NPP) satellite," IEEE Trans. Geosci. Remote Sens., 52, 1142–1156 (2014).
3. M.S. Goldberg, et al., "Associations between ambient air pollution and daily mortality among elderly persons in Montreal," Quebec Sci. Total Environ., 463–464 (2013), pp. 931-942 (2013).
4. M. Wang, X. Liu, L. Tan, L. Jiang, S. Son, W. Shi, K. Rausch, and K. Voss, "Impacts of VIIRS SDR performance on ocean color products", J. Geophys. Res. Atmos., 118, 10347-10360 (2013).
5. S. R. Signorini, B. A. Franz, C. R. McClain, "Chlorophyll variability in the oligotrophic gyres: mechanisms, seasonality and trends," Front. Mar. Sci. 2:1. doi: 10.3389/fmars.2015.00001.
6. S. Yoder, C. Doney, D. A. Siegel, and C. Wilson, "Study of marine ecosystem and biogeochemistry now and in the future: Example of the unique contributions from the space," Oceanography, 23, 104-117 (2010)
7. IOCCG (2018), "Earth Observations in Support of Global Water Quality Monitoring," Greb, S., Dekker, A., and Binding, C. (eds.), IOCCG Report Series, No. 17, International Ocean-Color Coordinating Group, Dartmouth, Canada. http://dx.doi.org/10.25607/OBP-113.
8. J. Sun and M. Wang, "On-orbit calibration of the Visible Infrared Imaging Radiometer Suite reflective solar bands and its challenges using a solar diffuser," Appl. Opt. 54, 7210-7223 (2015).
9. Cardema, J. C.; Rausch, K.; Lei, N.; Moyer, D. I.; DeLuccia, F. Operational calibration of VIIRS reflective solar band sensor data records, Proc. SPIE, 8510, 851019, 2012.
10. Lei, N.; Wang, Z.; Fulbright, J.; Lee, S.; McIntire, J.; Chiang, K.; Xiong, X. Initial on-orbit radiometric calibration of the Suomi NPP VIIRS reflective solar bands, Proc. SPIE, 8510, 851018, 2012.
11. J. Sun and M. Wang, "Visible Infrared imaging radiometer suite solar diffuser calibration and its challenges using solar diffuser stability monitor", Appl. Opt. 53, 8571-8584 (2014).
12. E. Hass, D. Moyer, F. DeLuccia, K. Rausch, J. Fulbright, "VIIRS solar diffuser bidirectional reflectance distribution function (BRDF) degradation factor operational trending and update," Proc. SPIE, 8510, 851016 (2012).
13. J. Fulbright, N. Lei, K. Chiang, X. Xiong, "Characterization and performance of the Suomi-NPP VIIRS solar diffuser stability monitor.," Proc. SPIE, 8510, 851015 (2012).
14. J. Sun, M. Chu, and M. Wang, "On-orbit characterization of the VIIRS solar diffuser and attenuation screens for NOAA-20 using yaw measurements", Appl. Opt., 57, 6605-6619 (2018).
15. Sun, J. and M. Wang, " NOAA-20 VIIRS reflective solar bands on-orbit calibration using solar diffuser and solar diffuser stability monitor", Proc. SPIE 10764, 107641C (2018).
16. Sun, J.; Xiong, X.; Butler, J. NPP VIIRS on-orbit calibration and characterization using the Moon, Proc. SPIE, 8510, 85101I, 2012.
17. Xiong, X.; Sun, J.; Fulbright, J.; Z. Wang; J. Butler, Lunar Calibration and Performance for S-NPP VIIRS Reflective Solar Bands, IEEE Trans. Geosci. Remote Sensing., 54, 1052-1061, 2016.
18. G. W. Kattawar, G. N. Plass, and J. A. Guinn, "Monte Carlo calculations of the polarization of radiation in the Earth's atmosphere–ocean system," J. Phys. Oceanogr., vol. 3, no. 4, pp. 353–372, Oct. 1973.
19. A. Ivanoff, "Polarization measurements in the sea," in Optical Aspects of Oceanography, N. G. Jerlov and E. S. Nielsen, Eds. London, U.K.: Academic, 1974, pp. 151–175.
20. R. C. Levy, L. A. Remer, and Y. J. Kaufman, Effects of neglecting polarization on the MODIS aerosol retrieval over land, IEEE Trans. Geosci. Remote Sensing, 42, 2576-2583, 2004.
21. G. Meister, E. J. Kwiatkowska, B. A. Franz, F. S. Patt, G. C. Feldman, and C. R. McClain, Moderate-resolution image spectroradiometer ocean color polarization correction, Applied Optics, 44, 5524-5535, 2005.
22. Kwiatkowska, E.J., B.A. Franz, G. Meister, C. McClain, and X. Xiong, Cross-calibration of ocean-color bands from Moderate Resolution

Imaging Spectroradiometer on Terra platform, Appl. Opt., 47, 6796-6810, 2008.
23. S. Huard, Polarization of Light, John Wiley & Sons, Chichester, 1997.
24. M. Born and E. Wolf, Principles of Optics, 7th edition, Cambridge University, 1999, ISBN 0-521-64222-1.
25. Gordon, H. R., T. Du, and T. Zhang, "Atmospheric correction of ocean color sensors: analysis of the effects of residual instrument polarization sensitivity", Appl. Opt., 36, 6938-6948 (1997).
26. M. Wang, "Aerosol polarization effects on atmospheric correction and aerosol retrievals in ocean color remote sensing," Appl. Opt., 45, 8951–8963, 2006.
27. Sun, J.; X. Xiong, "MODIS polarization sensitivity analysis", IEEE Trans. Geosci. Remote Sens., 45, 2875-2885, 2007.
28. Sun, J., X. Xiong, E. Waluschka, and M. Wang, "Suomi National Polar-Orbitting Partnership Visible Infrared Imaging Radiometer Suite polarization sensitivity analysis", Appl. Opt., 55, 7645-7658 (2016).
29. J. McIntire, et al, Monochromatic measurements of the JPSS-1 VIIRS polarization sensitivity, Appl. Opt., 55, 7444-7454 (2016).
30. D. Moyer, J. McIntire, J. Young, J. K. McCarthy, E. Waluschka, X. Xiong, and Frank J. De Luccia, "JPSS-1 VIIRS pre-launch polarization testing and performance", IEEE Trans. Geosci. Remote Sens., 55, 2463-2476 (2016).
31. Raytheon SBRS, Sensor Specification for Visible/Infrared Imager Radiometer Suite (VIIRS), PS154640-101B, February 2004.
32. H. Oudrari, J. McIntire, X. Xiong, J. Butler, J. Qiang, T. Schwarting, S. Lee, and B. Efremova "JPSS-1 VIIRS Radiometric Characterization and Calibration Based on Pre-Launch Testing." Remote Sensing, 8, 41 (2016).
33. G. N. Plass and G. W. Kattawar, "Polarization of the Radiation Reflected and Transmitted by the Earth's Atmosphere", Appl. Opt., 9, 1122-1130 (1970).
34. Nathan J. Pust and Joseph A. Shaw, "Wavelength dependence of the degree of polarization in cloud-free skies: simulations of real environments", OPTICS EXPRESS, 20, 15559-15568 (2012).
35. W. Sun, R. R. Baize, C. Lukashin, and Y. Hu, "Deriving polarization properties of desert-reflected solar spectra with PARASOL data", Atmos. Chem. Phys., 15, 7725–7734 (2015).
36. Sun, W. and Lukashin, C.: Modeling polarized solar radiation from the ocean–atmosphere system for CLARREO intercalibration applications, Atmos. Chem. Phys., 13, 10303–10324 (2013).
37. Nadal, F. and Breon, F.-M.: Parameterization of surface polarized reflectance derived from POLDER spaceborne measurements, IEEE T. Geosci. Remote Sens., 37, 1709–1718 (1999).
38. F. Maignan, F. M. Breon, E. Fedele, and M. Bouvier, "Polarized reflectances of natural surfaces: Spaceborne measurements and analytical modeling", Remote Sens. Environ., 113, 2642–2650, 2009.
39. H. Chen and C. R. N. Rao, "Polarization of light on reflection by some natural Surfaces", Brit. J. Appl. Phys., 1, 1191-1120 (1968).
40. P. Y. Deschamps, F. M. Bréon, M. Leroy, "Podaire, A., Bricaud, A., Buriez, J. C., and Sèze, G.: The POLDER mission: Instrument characteristics and scientific objectives", IEEE T. Geosci. Remote Sens., 32, 598–615 (1994).
41. J. W. Strutt, "XV. On the light from the sky, its polarization and colour", The London, Edinburgh, and Dublin Philosophical Magazine and Journal of Science, 41, 107–120 (1871).
42. L. Rayleigh, Lord, "XXXIV. On the transmission of light through an atmosphere containing small particles in suspension, and on the origin of the blue of the sky", The London, Edinburgh, and Dublin Philosophical Magazine and Journal of Science, 47, 375–384 (1899).
43. A. T. Young, "Rayleigh scattering". Applied Optics. 20, 533–5 (1981).
44. A. Bucholtz, "Rayleigh-scattering calculations for the terrestrial atmosphere", Appl. Opt., 34, 2765-2773 (1995).
45. M. Wang, "The Rayleigh lookup tables for the SeaWiFS data processing: Accounting for the effects of ocean surface roughness", Int. J. Remote Sens., 23, 2693-2702 (2002).
46. Wang, M., "A refinement for the Rayleigh radiance computation with variation of the atmospheric pressure", Int. J. Remote Sens., 26, 5651-5663 (2005).
47. Wang, M., "Rayleigh radiance computations for satellite remote sensing: accounting for the effect of sensor spectral response function", Opt. Express, 24, 12414-12429 (2016).
48. E. Waluschk, J. McCorkel, J. McIntire, and K. J. Thome, "VIIRS/J1 polarization narrative", Proc. SPIE, 9607, 960712 (2015).
49. Wang, M. and S. W. Bailey, "Correction of the sun glint contamination on the SeaWiFS ocean and atmosphere products", Appl. Opt., 40, 4790-4798 (2001).
50. Gordon, H. R and M. Wang, "Retrieval of water-leaving radiance and aerosol optical thickness over the oceans with SeaWiFS: A preliminary algorithm", Appl. Opt., 33, 443-452 (1994).
51. Gordon, H. R. and M. Wang, "Influence of oceanic whitecaps on atmospheric correction of ocean-color sensors," Appl. Opt., 33, 7754–7763 (1994).
52. IOCCG (2010), "Atmospheric Correction for Remotely-Sensed Ocean-Colour Products" this link opens in a new window, Wang, M. (ed.), Reports of International Ocean-Color Coordinating Group, No. 10, IOCCG, Dartmouth, Canada. https://dx.doi.org/10.25607/OBP-101
53. J. Sun and M. Wang, "NOAA-20 VIIRS reflective solar bands on-orbit calibration using solar diffuser and solar diffuser stability monitor", Proc. SPIE 10764, 107641C (2018).
54. J. Sun and M. Wang, "NOAA-20 VIIRS on-orbit calibration and characterization using the Moon," Proc. SPIE 10764, Earth Observing Systems XXIII, 107640U (2018).
55. M. Wang, " Remote sensing of the ocean contributions from ultraviolet to near-infrared using the shortwave infrared bands: simulations ", Appl. Opt., 46, 1535-1547 (2007).